Article

Not peer-reviewed version

Carbon Quantum Dots Doped $Ni_3Se_4/Co_9Se_8/Fe_3O_4$ Multilayer Nanosheets Prepared by One-Step Solvothermal Method to Boost Electrocatalytic Oxygen Evolution

Yao Zhang , Runze Wang , Longqi Zhu , Xu Li , Caixia Sun , Haizhen Liu , Lei Zhu , Kuikui Wang *

Posted Date: 23 May 2023

doi: 10.20944/preprints202305.1611.v1

Keywords: oxygen evolution reaction; transition metal selenides; multilayer nanosheets; carbon quantum dots; Heterostructures

Article

Carbon Quantum Dots Doped $Ni_3Se_4/Co_9Se_8/Fe_3O_4$ Multilayer Nanosheets Prepared by One-Step Solvothermal Method to Boost Electrocatalytic Oxygen Evolution

Yao Zhang [1,4], Runze Wang [1], Longqi Zhu [1], Xu Li [3], Caixia Sun [4], Haizhen Liu [5], Lei Zhu [2,*] and Kuikui Wang [1,*]

[1] Institute of Materials for Energy and Environment, Laboratory of New Fiber Materials and Modern Textile, Growing Basis for State Key Laboratory, College of Materials Science and Engineering, Qingdao University, Qingdao 266071, China
[2] College of Basic Medical, Qingdao Binhai University, Qingdao 266555, China
[3] Material Corrosion and Protection Key Laboratory of Sichuan province, Zigong, 643000, China
[4] Key Laboratory of New Metallic Functional Materials and Advanced Surface Engineering in Universities of Shandong, School of Mechanical and Electronic Engineering, Qingdao Binhai University, Qingdao 266555, Shandong, China
[5] MOE Key Laboratory of New Processing Technology for Non-ferrousMetals and Materials, Guangxi Key Laboratory of Processing for Non-ferrous Metals and Featured Materials, Guangxi University, Nanning, Guangxi 530004, China
* Correspondence: zhulei.126@163.com (L.Z.); kkwang@qdu.edu.cn (K.W.)

Abstract: Oxygen evolution reaction is a momentous part of electrochemical energy storage and conversion devices such as rechargeable metal-air batteries. It is particularly urgent to develop low-cost and efficient electrocatalysts for oxygen evolution reactions. As a potential substitute for noble metal electrocatalysts, transition metal selenides are still challenging in improving the activity of oxygen evolution reaction and the research of reaction intermediates. In this study, a simple one-step solvothermal method was used to prepare a polymetallic compound carbon matrix composite ($Co_9Se_8/Ni_3Se_4/Fe_3O_4$@C) with a multilayered nanosheets structure. It exhibited good OER activity in an alkaline electrolyte solution with an overpotential of 268 mV at 10 mA/cm^2. Besides, this catalyst also showed excellent performance in the 24 hours stability test. The composite presents a multi-layer sheet structure, which effectively improves the contact between the active site and the electrolyte. The selenide formed by Ni and Co has a synergistic effect, Fe_3O_4 and Co_9Se_8 form a heterojunction structure, which can effectively improve the reaction activity by initiating the electronic coupling effect through the interface modification. In addition, carbon quantum dots have rich heteroatoms and electron transferability, which improves the electrochemical properties of the composites. This work provides a new strategy for the preparation of highly efficient OER electrocatalysts utilizing the multimetal synergistic effect.

Keywords: oxygen evolution reaction; transition metal selenides; multilayer nanosheets; carbon quantum dots; Heterostructures

1. Introduction

Electrochemical energy storage and conversion device are considered to be one of the sustainable development technologies in the future [1,2]. Oxygen evolution reaction plays a key role in the application of energy storage and conversion devices, such as industrial water electrolyzers and rechargeable metal-air batteries [3,4]. Noble metal catalysts such as Iridium/Ruthenium oxide have the best overall catalytic performance in OER, but their limited availability and exorbitant price limit their extensive development and application [5–7]. Therefore, it is an urgent assignment to develop non-noble metal electrocatalysts to improve the catalytic activity of oxygen evolution reactions. Transition metal-based electrocatalysts have good competitive activity and toxicity

 doi:10.20944/preprints202305.1611.v1

resistance in alkaline medium. Because of its excellent stability and abundant reserves, it has become a research hotspot to replace Ruthenium/Iridium-based electrocatalysts. Numerous studies have shown that the use of polymetallic-based electrocatalysts can achieve high efficiency by optimizing adsorption energy, increasing stability and the electrical conductivity of the electrocatalyst [8,9]. In addition, carbon quantum dots (CQDs), as zero-dimensional carbon nanomaterials, have great potential in electrochemistry due to their fast electron transfer ability and rich specific surface area, and their abundance of heteroatoms (O, N, S) can provide ideal active sites for electrochemical behavior [10].

Transition metal hydroxide [11,12], oxide [13,14], sulfide [15,16], selenide [17,18], phosphate [19–21] and other electrocatalysts have great potential in the field of electrocatalyst application. As an electrocatalyst, the activity of oxygen sulfide is much higher than that of pure oxide or sulfide [22–24]. Transition metal selenides and their composite materials have been widely concerned in catalysis, electrochemistry, and other fields due to their complex physical and chemical properties. Thanks to the metal properties of Se, selenides have higher conductivity than corresponding oxides and sulfides [25,26]. MOOH is generally considered an important active intermediate in the oxygen evolution reaction of transition metal selenides [27,28]. Compared with a single metal-based electrocatalyst, a multi metal-based electrocatalyst shows higher electrocatalytic activity for oxygen evolution reaction. For example, it has been reported that MoCoNiS is generated by introducing Mo into Co-based electrocatalysts. The polymetallic-based electrocatalysts show excellent oxygen evolution reaction activity and cycle stability, indicating that there is a synergistic effect between different heteroatoms [29].

Among the transition metal-based electrocatalysts, Ni-based, Fe-based electrocatalysts have attracted much attention because of their general availability, and the Co element tends to play a role in bimetallic based electrocatalysts, forming a synergistic effect with other transition metals and bringing about the improvement of catalytic activity for oxygen evolution reaction [30–32]. By introducing other transition metal compounds to form multi metal-based electrocatalysts, the catalytic activity of oxygen evolution reaction can be effectively improved. Polymetallic selenides, such as iron-nickel and iron-cobalt selenide, have been proven to be efficient non-noble metal OER electrocatalysts [33,34]. They are in situ transformed into highly active polymetallic oxides in alkaline electrolytes, and synergistic effects occur between different active sites. Du et al. used a one-step hydrothermal method to grow cobalt selenide coated nickel selenide nanorods in situ on a nickel foam substrate, which showed excellent OER performance in an alkaline environment. This study confirmed that NiOOH/CoOOH is instrumental to achieve excellent cycle stability in the alkaline medium in oxygen evolution reaction, and the synergistic effect between CoSe and NiSe balances the formation of NiOOH/CoOOH heterostructures and exposes more active sites [35]. Liu et al. prepared $Co_xNi_{1-x}Se_2$ nanoparticle film on a conductive Ti plate by electrodeposition method, which is an excellent bi-functional catalyst. In the selenide formed by Co ions and Ni ions, Co atoms and Ni atoms form a synergistic effect, which significantly improves the oxygen evolution reaction efficiency [36]. Du et al. prepared Fe-doped Ni_3Se_4 layered nanosheets by solvothermal method and topological transformation. During the oxygen evolution reaction, Fe atoms maintain electronic conductivity between the electrode and the metal hydroxide layer, which provides rapid charge transfer and improves OER activity, with an overpotential of only 225 mV at a current density of 10 mA cm^{-2} [37]. In addition, it was reported that the bond energy of the Co-O bond in OER intermediate CoOOH was reduced by loading Fe_3O_4 on the surface of Co_9S_8, and the OER activity was effectively increased [38]. Due to the poor conductivity of some transition metal compounds, their development in the field of electrocatalysis of oxygen evolution reactions is limited. It is reported that the material's electrical conductivity was improved by combining carbon quantum dots with transition metal compounds, and the reaction rate of oxygen evolution was significantly improved [39]. Hybrid electrocatalysts with highly conductive interconnected carbon frameworks can maintain electrical connections with catalytic active species. Polymetallic selenide carbon matrix composites are expected to improve electrocatalytic performance.

 doi:10.20944/preprints202305.1611.v1

Based on these studies, a simple one-step hydrothermal method was used to prepare carbon quantum dots doped polymetallic compound composite with multilayer nanocrystalline sheets ($Co_9Se_8/Ni_3Se_4/Fe_3O_4$@C). The involvement of carbon quantum dots significantly improves the electron transport efficiency of the synthesized materials. Among the selenides formed, multiple metal elements produced a synergistic effect. Fe_3O_4 and Co_9Se_8 form a heterojunction structure, which can effectively improve the reaction activity by initiating the electronic coupling effect through the interface modification. The addition of Fe_3O_4 reduced the adsorption energy of the Co group and O group at the active site, further reducing the activation energy. It shows an overpotential of 268 mV at a current density of 10 mA cm^{-2} and a Tafel slope of 64 mV dec^{-1}. These results provide new ideas and suggestions for transition metal selenides to become excellent OER electrocatalysts.

2. Experimental

2.1. Preparation of N-doped carbon quantum dots solution

Dissolve 1.05 g citric acid monohydrate and 0.9 g urea in 25 mL distilled water, stir for 30 min, transfer to 100 mL Teflon lined stainless steel autoclave, and keep it warm at 150 °C for 6 h. After cooling to room temperature and centrifuging at 8000 rpm for 10 minutes, take the solid part and evenly disperse it in distilled water to obtain carbon dots solution.

2.2. Preparation of $Co_9Se_8/Ni_3Se_4/Fe_3O_4$@C

Dissolve 4 g of sodium hydroxide in the mixed solution (10 mL of distilled water and 30 mL of ethanol), add 0.16 g of selenium powder and stir, heat the mixed solution during stirring until the selenium powder is completely dissolved to form solution A. Dissolve 1.2 mmol cobalt chloride hexahydrate, 0.4 mmol nickel chloride hexahydrate and 0.4 mmol ferrous sulfate heptahydrate in 0.25 M EDTA solution (solvent is 5 mL distilled water and 5 mL carbon quantum dots solution) to obtain solution B. After mixing solution A and solution B, add 7 mL hydrazine hydrate drop by drop, transfer the mixed solution to 100 mL Teflon lined stainless steel autoclave and keep it warm at 180 °C for 20 h. The black precipitate collected after cooling to room temperature was thoroughly washed with dilute acid and distilled water, then dried at 60 °C for 12 h to obtain the target product.

2.3. Characterization

The crystal structure of the as-prepared samples was characterized by X-ray diffraction (Rigaku Ultima IV X-ray diffractometer equipped with Cu Ka radiation) at room temperature. The morphology and elemental mapping of the samples were observed by field emission scanning electron microscopy (FESEM, JEOLJSM7800F), with energy dispersive spectrometer (EDS). The crystal structure of the materials was characterized by high-resolution transmission electron microscopy (TEM, JEOLJEM-2100). X-ray photoelectron characterization was recorded on a Thermo scalable 250Xi electron spectrometer system (XPS) using Al Ka radiation. The specific surface area of the sample was measured by Brunauer-Emmett-Teller (BET).

2.4. Electrochemical measurement

All the electrochemical measurements, including (LSV, EIS, Cdl, CP) were carried out in the electrochemical workstation (CHI660E, CH Instrument), using Pt as the counter electrode, Hg/HgO electrode as reference electrode, glass carbon electrode as working electrode, 1.0 M KOH solution as electrolyte. The working electrode was prepared by adding the 5 mg sample to a mixed solution of 600 μl ethanol, 380 μl ultra-pure water and 20 μl 5w% Nafion solution. Then, the mixed solution containing the catalyst sample is ultrasonic for 30 min to form a well-dispersed suspension. The dispersed catalyst was then dripped onto the glassy carbon electrode (3 mm diameter and 0.35 mg cm^{-2} in loading). According to the Nernst equation (E (RHE) = E (Hg/HgO) + 0.924), the working potential is converted into reversible hydrogen potential, and the OER overpotential is calculated by

Preprints (www.preprints.org) | NOT PEER-REVIEWED | Posted: 23 May 2023 doi:10.20944/preprints202305.1611.v1

η (V) = E (RHE)-1.23 V. For stability test, take 400 μl solution is dropped on the 1 cm*1 cm foam nickel matrix, dried and placed on the electrode clamp as the working electrode.

3. Results and Discussion

$Co_9Se_8/Ni_3Se_4/Fe_3O_4$@C was synthesized by a simple one-step hydrothermal method (Figure 1a). Co_9Se_8 sample is at the XRD diffraction peaks near 28.22°, 29.66°, 45.14°, 49.38° and 58.56° correspond to (311), (222), (511), (440) and (622) crystal planes. The Ni_3Se_4 component in the sample is the XRD diffraction peaks near 25.28°, 29.76°, 31.14°, 36.19°, 47.70°, 52.07°, 61.89° and 64.98° correspond to (220), (311), (222), (400), (511), (440), (622) and (444) crystal planes. Fe^{2+} ions are oxidized to Fe^{3+} ions by oxygen in the air. Because the solution is alkaline during the preparation process when the hydrothermal temperature reaches 160 °C, Fe ions participate in the reaction, and OH^- ions in the solution form Fe_3O_4. The Fe_3O_4 component in the sample is in the XRD diffraction peaks near 30.06°, 35.45°, 37.12°, 43.04°, 57.17° and 62.73° correspond to (220), (311), (222), (400), (511) and (440) crystal planes. Figure 1b–d show the cell structures of Co_9Se_8, Ni_3Se_4 and Fe_3O_4, in which unsaturated metal atoms involved in surface coordination are exposed to the crystal periphery, providing adsorption active sites for intermediates in electrocatalytic processes [40]. In Figure 1a, the overall peak of XRD shifts to the right because the lattice is doped with larger heteroatoms than the host atoms, which will lead to smaller cell parameters and shift the peak position to the right [41]. Figure S1 shows the XRD diagram of the synthetic samples under different transition metal salt feed ratios. By comparing XRD standard cards, it is found that there is no difference in the chemical composition of the final product synthesized under different metal molar ratios. However, by comparing the corresponding XRD peak intensities of different substances, it is found that the proportion of different chemical components is different.

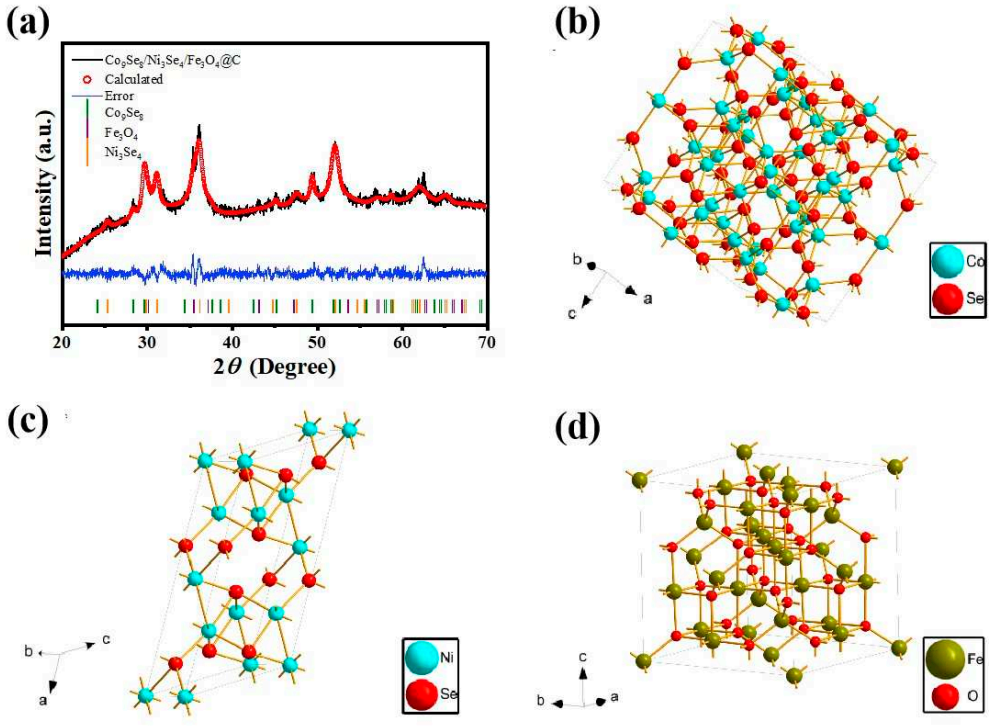

Figure 1. (a) XRD patterns of $Co_9Se_8/Ni_3Se_4/Fe_3O_4$@C, (b) the unit cell of Co_9Se_8, (c) the unit cell of Ni_3Se_4, (d) the unit cell of Fe_3O_4.

In addition, the $Co_9Se_8/Ni_3Se_4/Fe_3O_4$@C sample was also measured by XPS measurement to show its near-surface element composition and chemical state. Figure 2b–f show the survey spectrum of the $Co_9Se_8/Ni_3Se_4/Fe_3O_4$@C sample. According to the attribution of the peaks in the measured

Preprints (www.preprints.org) | NOT PEER-REVIEWED | Posted: 23 May 2023 doi:10.20944/preprints202305.1611.v1

spectrum, the chemical composition of the $Co_9Se_8/Ni_3Se_4/Fe_3O_4$@C sample in the near-surface range are Ni, Co, Fe, C and Se (O element comes from the inevitable air surface adsorption).

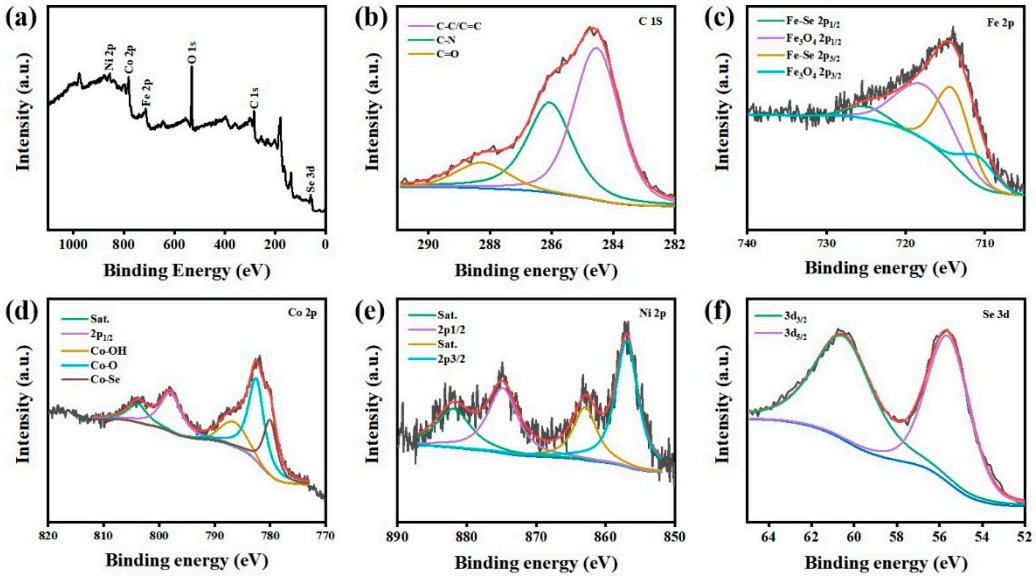

Figure 2. (a) XPS spectrum of $Co_9Se_8/Ni_3Se_4/Fe_3O_4$@C, High-resolution XPS of (b) C 1s, (c) Fe 2p, (d) Co 2p, (e) Ni 2p and (f) Se 3d.

The result is shown in Figure 2, The signal peak at 803.83 eV represents a satellite peak of Co $2p_{1/2}$, while the signal peak at 797.92 eV represents a Co $2p_{1/2}$ orbit. The signal peaks at 786.5 eV and 782.51 eV represent the presence of Co-OH and Co-O bonds, respectively, while the signal peaks at 780 eV represent the Co-Se bonds of the Co_9Se_8 phase in Figure 1a [38]. The Ni 2p high-resolution spectrum shows that two notable peaks at 874.81 and 856.94 eV, which are assigned to the Ni $2p_{1/2}$ and Ni $2p_{3/2}$ signals of Ni, accompanying two shake-up satellite peaks (marked as "Sat."). This indicated the presence of Ni^{3+} and Ni^{2+} ions (Figure 2e) [42]. The spectrum of Fe 2p consists of two spin orbit states generated by $2p_{3/2}$ and $2p_{1/2}$ signals. The signal peaks of Fe at 717.5 eV and 710 eV correspond to the $2p_{3/2}$ and $2p_{3/2}$ orbitals of Fe, respectively, and correspond to the mixed oxidation states of Fe^{2+} and Fe^{3+} in Fe_3O_4. The signal peaks at 725 eV and 713.9 eV correspond to Fe-Se bonds in the compound, respectively [38]. The signal peaks located at 60.49 eV and 55.59 eV represent Se $3d_{3/2}$ and Se $3d_{5/2}$ orbits, respectively (Figure 2f) [43]. Expressed as C-C or C=C at 288.25 eV expressed as C-N at 286.05 eV, interpreted as N element doped in carbon quantum dots, expressed as C=O at 284.54 eV, through the analysis of the XPS spectrum (Figure 2b) [44]. This is consistent with the XRD results, it can be judged as the successful synthesis of $Co_9Se_8/Ni_3Se_4/Fe_3O_4$@C (Figure 1a).

As shown in Figure 3a–d, the catalyst $Co_9Se_8/Ni_3Se_4/Fe_3O_4$@C prepared presents multi-layer nanosheets layered structure on the micro-size, and has bulges and folds on the surface of the layered structure. Figure 3c shows the layered structure of multilayer nanosheets from another perspective, and the material has a rich pore structure. This provides rich active sites for the catalytic process and effectively improves the catalytic efficiency. As shown in Figure 3e,f, Fe, Co, Ni and Se are uniformly distributed in the thin sheet, indicating that Co_9Se_8, Ni_3Se_4 and Fe_3O_4 form uniform thin sheets rather than separate to form their own structure. Because Fe_3O_4 has excellent dielectric, magnetic and electrical conductivity, as shown in Figure 3f, the Fe element is uniformly distributed on the material surface, which brings excellent electron transfer efficiency to the catalyst [38].

Preprints (www.preprints.org) | NOT PEER-REVIEWED | Posted: 23 May 2023 doi:10.20944/preprints202305.1611.v1

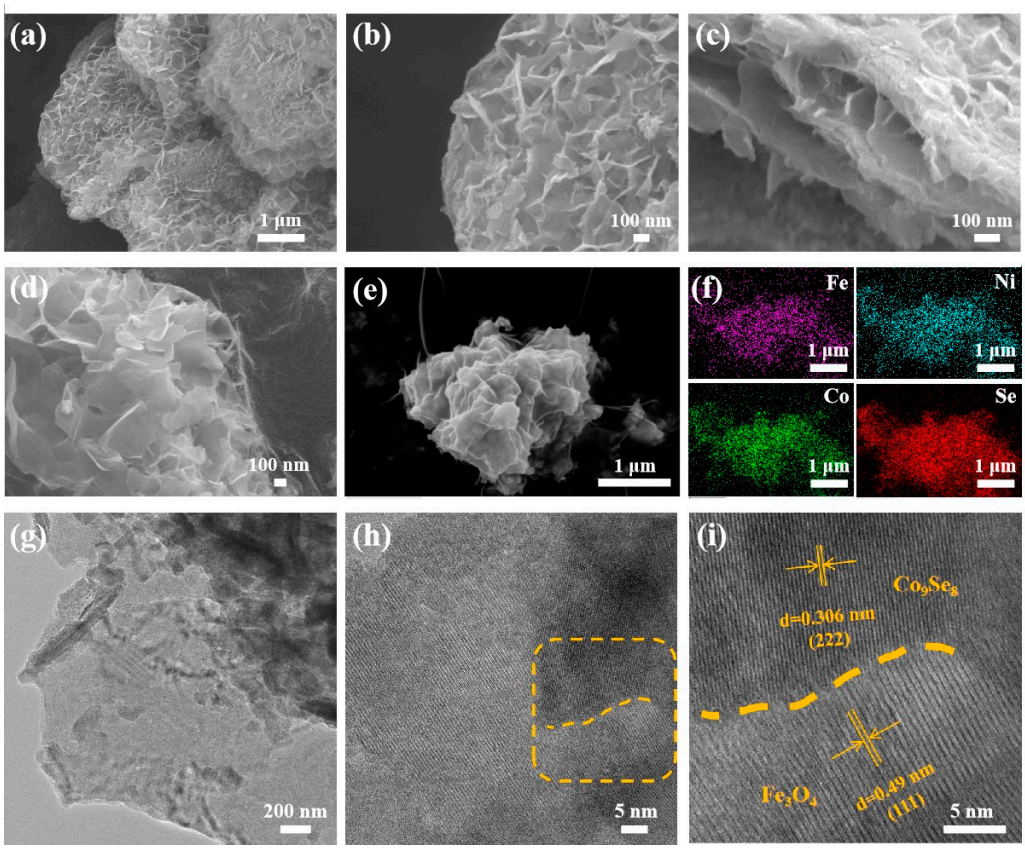

Figure 3. (a-d) SEM images of $Co_9Se_8/Ni_3Se_4/Fe_3O_4$@C, (e,f) EDS elemental mapping of $Co_9Se_8/Ni_3Se_4/Fe_3O_4$@C, (g-i) TEM images of $Co_9Se_8/Ni_3Se_4/Fe_3O_4$@C.

Figure 3g shows the TEM image of the main sample C_9Se_8 at low magnification, and it can be seen that the sample presents an obvious single-layer nanosheets structure, which is consistent with the multi-layer nanosheets structure shown in Figure 3a–d. Under the action of ultrasound, the multi-layer nanosheets structure is destroyed and the single-layer nanosheet structure is retained, which can more clearly show the size and thickness uniformity of the nanosheets. Figure 3h,i show the heterojunction structure and local enlargement at high magnification. The lattice stripe spacing of the (222) plane of Co_9Se_8 is 0.306 nm, and the lattice stripe spacing of the (111) plane of Fe_3O_4 is 0.49 nm. The obvious phase boundary between crystals confirms the successful formation of the heterojunction. At the same time, it can be seen from Figure 3a–d, there are folds on the surface of the thin section, which also leads to the increase of the distance between layers of the multilayer structure, which plays a positive role in increasing the specific surface area of the sample. The specific surface area and pore structure of the prepared $Co_9Se_8/Ni_3Se_4/Fe_3O_4$@C were characterized by nitrogen adsorption/desorption isotherms. Isotherms show porous characteristics (Figure S2). A large specific surface area and porous structure may provide more exposed active sites and accessible channels for electrocatalysis. The specific surface area and pore structure of $Co_9Se_8/Ni_3Se_4/Fe_3O_4$@C were characterized by nitrogen adsorption/desorption isotherms. Nitrogen adsorption/desorption isotherms are typical type IV isothermal adsorption/desorption curves. Its specific surface area reaches 32.158 m^2/g. As shown in Figure S3, the pore size is mainly distributed at about 30 nm, and the larger specific surface area and porous structure of the material may provide more accessible channels for the electrolyte, and more exposed active sites for the electrocatalysis process.

The electrocatalytic performance of $Co_9Se_8/Ni_3Se_4/Fe_3O_4$@C is estimated by linear sweep voltammetry (LSV), which uses a three-electrode structure to test in 1.0 M KOH solution. In Figure 4a, redox peaks appear at different potentials. Due to the generation of redox peaks caused by the oxidation of low valence metal ions, Co^{2+} and Ni^{3+} ions change to high valence and evolve into Co^{3+} and Ni^{4+} ions. The relationship between the different molar ratios of transition metal FeCoNi and the lowest overpotential is studied, as shown in Figure 4a, it can be found that $Co_9Se_8/Ni_3Se_4/Fe_3O_4$@C

Preprints (www.preprints.org) | NOT PEER-REVIEWED | Posted: 23 May 2023 doi:10.20944/preprints202305.1611.v1

(metal element ratio is Fe:Co:Ni=1:3:1). It exhibits a minimum overpotential of 268 mV at 10 mA/cm^2, which exceeds that of commercial ruthenium oxide and other samples of different proportions. The corresponding Tafel curves of electrocatalysts with different transition metal element ratios are shown in Figure 4b. Compared with other samples in this study, the Tafel slope of $Co_9Se_8/Ni_3Se_4/Fe_3O_4$@C (metal element ratio is Fe:Co:Ni=1:3:1) is 64 mV dec^{-1}, which is much lower than commercial ruthenium oxide (224 mV dec^{-1}) and other samples with different proportions, indicating that the reaction kinetics is faster. This is because Co_9Se_8 and Fe_3O_4 form an effective interphase interface engineering. The interface formed by Co_9Se_8 and Fe_3O_4 can be clearly seen, the upper part is the (222) crystal plane of Co_9Se_8 phase, and the lower part is the (111) crystal plane of Fe_3O_4 phase. The obvious boundary of the two phases can be clearly observed in the middle. Thanks to the interface modification, the electron-coupling interaction enhances the oxygen evolution reaction activity. The oxygen evolution reaction activity of the material has been greatly improved [46,47]. At the same time, the 3D nanosheets ensures a rich exposure of active sites and accelerates the reaction kinetics. The double-layer capacitance is measured by cyclic voltammetry (CV) to estimate the electrochemical surface area (ECSA). A sample with a metal element ratio of Fe:Co:Ni=1:3:1 has a capacitance of 3.7 mF/cm^2 (Figure S4–S6). This can be attributed to the participation of Fe and Ni transition metals, as well as the unique structure of the multilayer nanosheets, which brings a larger specific surface area, and the increase in crystal strain caused by the tiny atomic radius difference between nickel and cobalt. The charge transfer resistance (Rct) reflects the difficulty of the step of charge transfer through the two-phase interface between the electrode and electrolyte solution during the electrode process. The electron transfer resistance (Rct) is measured by electrochemical impedance spectroscopy. The Nyquist diagram shows that among the samples with different metal ratios and ruthenium oxide, the sample with the metal element ratio of Fe:Co:Ni=1:3:1 has the lowest ohmic resistance of 1.44 Ω cm^2 (Figure 4d). Low Rct means that the electron transfer at the catalyst and electrolyte interface is much faster, and small Rct means good electrical conductivity, both of which are attributed to the combination of carbon quantum dots that improves the overall electrical conductivity of the material.

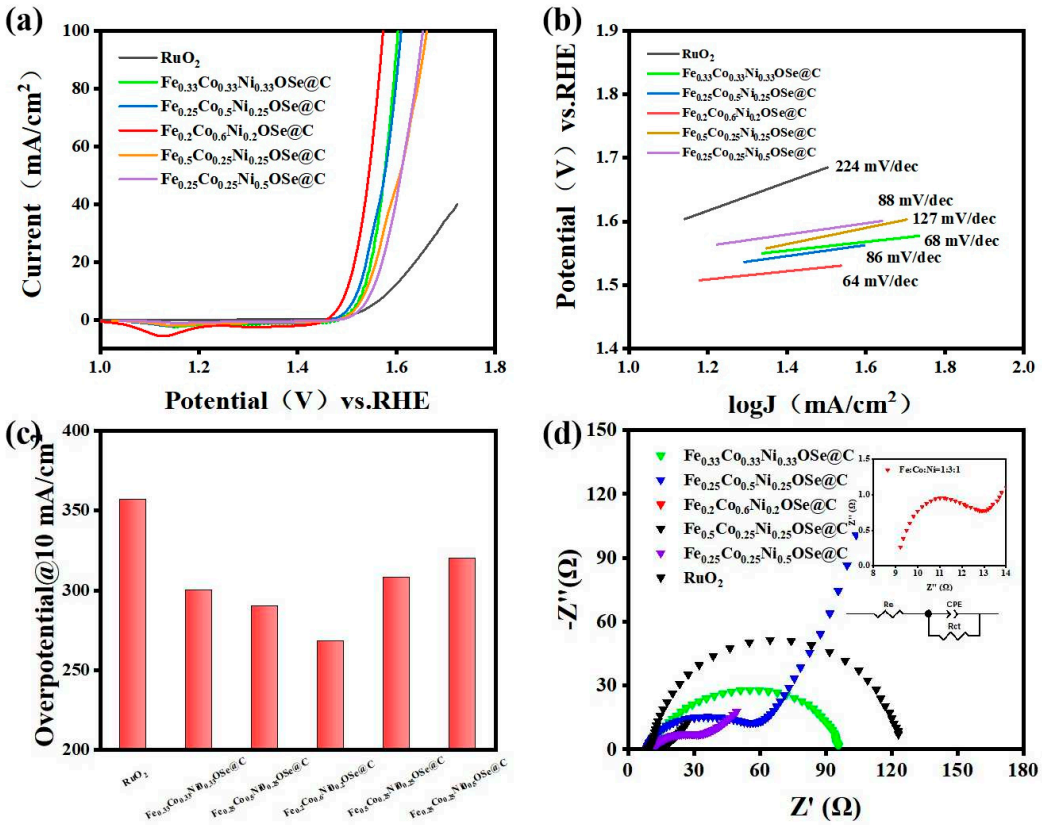

Preprints (www.preprints.org) | NOT PEER-REVIEWED | Posted: 23 May 2023 doi:10.20944/preprints202305.1611.v1

Figure 4. (a) The polarization curves of the as-prepared catalyst at a scan rate of 10 mV s-1 for OER in 1.0 M KOH, (b) Tafel plots of as-prepared catalyst in 1.0 M KOH, (c) Overpotential of different electrocatalysts at 10 mA/cm^2, (d) Nyquist plots of different electrocatalysts.

The $Co_9Se_8/Ni_3Se_4/Fe_3O_4$@C electrocatalytic performance was estimated by linear sweep voltammetry (LSV), which was tested in a 1.0 M KOH solution with a three-electrode structure. The relationship between different molar ratios of transition metal FeCoNi and the lowest overpotential was studied. In order to facilitate discrimination, the samples prepared with different metal element ratios were recorded as $Fe_xCo_yNi_zOSe$@C (for example, a sample prepared with a metal element ratio of Fe: Co: Ni = 1:3:1 is recorded as $Fe_{0.2}Co_{0.6}Ni_{0.2}OSe$@C). Under the same experimental conditions, with the increase of Co atoms feeding ratio, the minimum overpotential of the sample at 10 mA/cm^2 current density in LSV gradually decreases and reaches the minimum overpotential when Fe: Co: Ni=1:3:1, which shows that in $Co_9Se_8/Ni_3Se_4/Fe_3O_4$@C for the oxygen evolution reaction on the sample, its catalytic active center should be the position of Co atoms, but the excessive ratio of Co atoms weakens the synergistic effect between Fe, Co and Ni, so there is an optimal ratio (Figure 4a). With the increase of the proportion of Co atoms, the micromorphology of the samples evolves from nanoparticles to multilayer nanoflakes (Figure 5a–d). In order to display the microstructure of the sample more clearly, an enlarged image has been added in Figure S7 to support the information. At the optimal ratio of Fe: Co: Ni = 1:3:1, the morphology of the sample presents the structure of multilayer nanosheets, which provides a better scheme for full contact with the electrolyte.

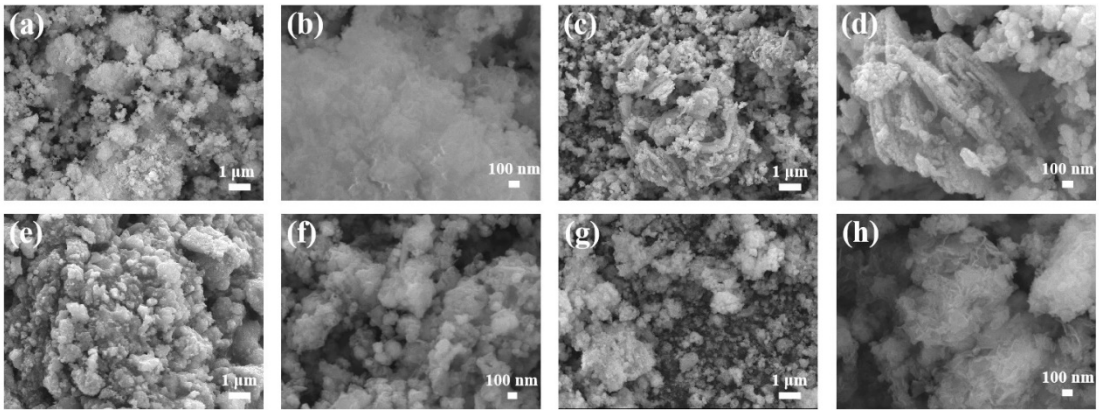

Figure 5. SEM images of $Co_9Se_8/Ni_3Se_4/Fe_3O_4$@C with different Co/Ni/Fe ratios: (a,b) $Fe_{0.33}Co_{0.33}Ni_{0.33}OSe$@C, (c,d) $Fe_{0.25}Co_{0.5}Ni_{0.25}OSe$@C, (e,f) $Fe_{0.5}Co_{0.25}Ni_{0.25}OSe$@C, (g,h) $Fe_{0.25}Co_{0.25}Ni_{0.5}OSe$@C.

When Fe or Ni elements are dominant metal elements, OER performance is found to be reduced, which further confirms that the Co group is the active site for the oxygen evolution reaction of samples. This is preliminarily consistent with the oxygen evolution reaction pathway of cobalt oxygen catalyst proposed by Mattioli et al. In several intermediate steps of oxygen evolution reaction, the last O_2 molecule is separated from Co active center, which may be the speed control step of cobalt-based catalysts [35]. The dominant position of the Fe atoms will lead to the synthesis of more particle structures in the micromorphology, which is not conducive to the increase of specific surface area and exposure of the active site. The dominant position of Ni atoms will lead to the formation of flower-like nanosheets, which is also not conducive to the full contact between the active site and electrolyte (Figure 5e–h). Studies have shown that the OER performance of Co_9S_8 grown on the go is significantly improved after the introduction of Fe on the surface of Co_9S_8 [38]. Se atom and S atom have the same outermost electron distribution and similar electronic structure. Fe_3O_4 has a mixed oxidation state of Fe^{3+} and Fe^{2+} ions, in which Fe^{2+} ion has a electronegativity of 1.83, lower than 1.88 of Co^{2+} ions. Electronegativity reflects the ability of atoms in elements to attract electrons in compounds. During the polarization process, Co^{2+} ions attract electrons around Fe^{2+}, causing Co to be in a low oxidation state, thereby promoting the fracture of Co-O bonds and the release of O_2,

 doi:10.20944/preprints202305.1611.v1

accelerating the activity of oxygen evolution reactions [32]. This also confirmed that with the participation of the Fe element, the OER performance of samples was improved, but the increase of the Fe component would lead to the reduction of Co species as catalytic active centers, and the reduction of exposed active sites would lead to the decline of OER performance. It is well-known that Fe^{3+} is the strongest transition metal based on lewis acid, Fe^{3+} ions have remarkable effects on changing the electronic properties of other metal cations. Ni species will be oxidized after polarization to form more Ni^{4+} cations, which will reduce the catalytic efficiency of the oxygen evolution reaction. The participation of Fe^{3+} ions will effectively inhibit the dynamic competition of the metal oxidation effect, which will lead to the enhancement of oxygen evolution reaction activity [45]. Ni atoms and Co atoms are involved in the formation of selenides, and the presence of Ni atoms makes the lattice of Co_9Se_8 slightly offset, which reduces the activation energy of intermediates generated in the OER process and improves the catalytic efficiency.

Using the same experimental method, single metal and bimetallic electrocatalysts were prepared for comparison. The oxygen evolution reaction parameters of the material were tested by a simple three-electrode system in 1.0 M KOH solution (Figure 6a–c). The catalytic activity of single metal and bimetallic electrocatalysts are significantly worse than that of a multi metal-based electrocatalyst. It is attributed to the interface modification that enhances the activity of oxygen evolution reaction due to the electron-coupling interaction. In Figure 6a, the introduction of Fe_3O_4 brings an obvious boost to the catalytic activity of the catalyst for the oxygen evolution reaction, which is attributed to the enhanced electron transport efficiency by Fe_3O_4, as well as the reduced bond energy of the oxygen evolution reaction intermediate MOOH. The participation of Fe_3O_4 can effectively inhibit the dynamic competition of the metal oxidation effect, that is, the transition of Ni ions to high valence during the polarization process. This will increase the catalytic activity of the oxygen evolution reaction. At the same time, carbon quantum dots have a large number of active site due to their rich heteroatoms. The combination with the catalyst material brings about active site for oxygen evolution reaction, which better improves the overall electron transport efficiency of the material [10]. The introduction of carbon quantum dots can significantly reduce the resistivity of the material, and the combined effect of Fe3O4 and carbon quantum dots effectively improves the overall electron transfer efficiency of the material (Figure 6d). Figure 6c shows the overpotential and Tafel slope histogram of different materials at a current density of 10mA/cm^2, which can more intuitively display the oxygen evolution reaction activity and reaction kinetics of different materials. The electric double-layer capacitance of different samples was measured and calculated by cyclic voltammetry (Figure S8–S11). It is found that the introduction of carbon quantum dots will reduce the electric double-layer capacitance of the product, but it has a better catalytic effect on the oxygen evolution reaction. In order to evaluate the chemical stability of the electrocatalyst, the material was kept in 1.0 M KOH solution for 24 hours at a constant current density of 10 mA/cm^2, and the material showed excellent stability (Figure 6e).

Preprints (www.preprints.org) | NOT PEER-REVIEWED | Posted: 23 May 2023 doi:10.20944/preprints202305.1611.v1

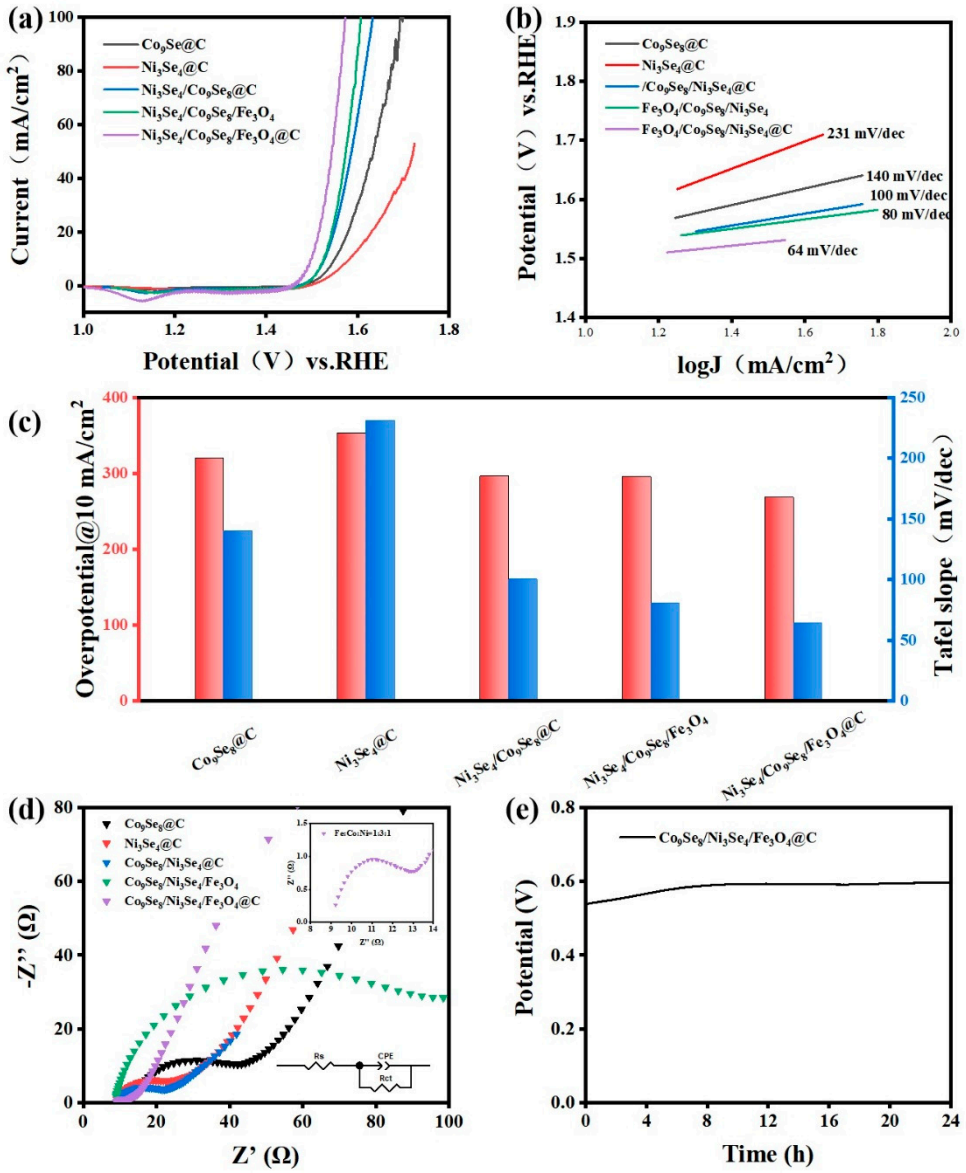

Figure 6. (a) The polarization curves of the as-prepared catalyst at a scan rate of 10 mV/s for OER in 1.0 M KOH, (b) Tafel plots of the as-prepared catalyst in 1.0 M KOH, (c) The overpotential and Tafel slope of the prepared catalyst in 1.0 M KOH at a scanning rate of 10 mV/s, (d) Nyquist plots of different electrocatalysts, (e) The voltage-time curve of the sample in 1.0 M KOH solution at a constant current density of 10 mA/cm² for 24 hours.

After 24 hours of the stability test, the micro-morphology of the sample has changed significantly (Figure S12). The multilayer nanosheets structure collapsed during a long time of polarization, and the thickness of the lamellar structure increased, which led to less contact with the electrolyte. This is the main reason for the increase of polarization voltage during the stability test. After the XPS test of the sample after the stability test (Figure S13), it is found that Se evolves into SeO_x species under strong polarization, and the signal peak of SeO_x can be observed, which is caused by the oxidation of Se under alkaline conditions. The signal peak of Fe element has no obvious change before and after the test, which is due to the good stability of Fe^{3+} ions in the oxygen evolution reaction process as the strongest Lewis acid [45]. In addition, the electrons of Ni and Co atoms can be transferred to Fe atoms to protect them from oxidation and transition to high oxidation state [32].

4. Conclusion

In summary, the $Co_9Se_8/Ni_3Se_4/Fe_3O_4$@C with a multilayer nanosheets structure prepared by a simple one-step hydrothermal method has an overpotential of 268 mV and a Tafel slope of 64 mV dec^{-1} at a current density of 10 mA cm^{-2}. First, the polymetallic selenide forms a highly active polymetallic oxide in the alkaline electrolyte, resulting in a synergistic effect of different active sites. Then, due to the structure of the multilayer nanosheets, more active sites are generated. The dots are exposed, which greatly improves the catalytic efficiency. Through the formation of effective interface engineering between the two phases, the oxygen evolution reaction activity of the material has been greatly improved. Due to the interface modification, the electron-coupling interaction enhances the oxygen evolution reaction activity, and the 3D nanosheets ensures a rich exposure of active sites and accelerates the reaction kinetics. Finally, since carbon quantum dots have abundant heteroatoms, they can provide more active sites for oxygen evolution reaction. After being compounded with transition metal selenides, they also improve the conductivity of the materials and the electron transfer efficiency in the catalytic process. This provides new insights into the design ideas for the future synthesis of high-efficiency and low-cost electrocatalysts.

Acknowledgments: The authors are grateful for financial support from the National Natural Science Foundation of China (51801108), the Key Research and Development Program of Shandong Province (2019GGX103048) and the Opening Project of Material Corrosion and Protection Key Laboratory of Sichuan province (2021CL18). This project is also supported by open foundation of State Key Laboratory of Featured Metal Materials and Life-cycle Safety for Composite Structures, Guangxi University (Grant No. 2022GXYSOF16).

References

1. Tian, X.; Lu, X.F.; Xia, B.Y.; Lou, X.W. Advanced Electrocatalysts for the Oxygen Reduction Reaction in Energy Conversion Technologies. *Joule* **2020**, *4*, 45–68. https://doi.org/10.1016/j.joule.2019.12.014.
2. Chang, H.; Shi, L.-N.; Chen, Y.-H.; Wang, P.-F.; Yi, T.-F. Advanced MOF-derived carbon-based non-noble metal oxygen electrocatalyst for next-generation rechargeable Zn-air batteries. *Co-ord. Chem. Rev.* **2022**, *473*, 214839. https://doi.org/10.1016/j.ccr.2022.214839.
3. Wang, H.; Zhu, S.; Deng, J.; Zhang, W.; Feng, Y.; Ma, J. Transition metal carbides in electrocatalytic oxygen evolution reaction. *Chin. Chem. Lett.* **2021**, *32*, 291–298. https://doi.org/10.1016/j.cclet.2020.02.018.
4. Lu, X.F.; Fang, Y.; Luan, D.; Lou, X.W.D. Metal–Organic Frameworks Derived Functional Materials for Electrochemical Energy Storage and Conversion: A Mini Review. *Nano Lett.* **2021**, *21*, 1555–1565. https://doi.org/10.1021/acs.nanolett.0c04898.
5. Ding, Y.; Cao, K.W.; He, J.W.; Li, F.M.; Huang, H.; Chen, P.; Chen, Y. Nitrogen-doped graphene aerogel-supported ruthenium nanocrystals for pH-universal hydrogen evolution reaction. *Chin. J. Catal.* **2022**, *43*, 1535–1543. https://doi.org/10.1016/j.jechem.2021.05.034.
6. Xue, Q.; Bai, X.-Y.; Zhao, Y.; Li, Y.-N.; Wang, T.-J.; Sun, H.-Y.; Li, F.-M.; Chen, P.; Jin, P.; Yin, S.-B.; et al. Au core-PtAu alloy shell nanowires for formic acid electrolysis. *J. Energy Chem.* **2022**, *65*, 94–102. https://doi.org/10.1016/j.jechem.2021.05.034.
7. Wang, T.; Jiang, Y.; He, J.; Li, F.; Ding, Y.; Chen, P.; Chen, Y. Porous palladium phosphide nanotubes for formic acid electrooxidation. *Carbon Energy* **2022**, *4*, 283–293. https://doi.org/10.1002/cey2.170.
8. Li, L.; Cao, X.; Huo, J.; Qu, J.; Chen, W.; Liu, C.; Zhao, Y.; Liu, H.; Wang, G. High valence metals engineering strategies of Fe/Co/Ni-based catalysts for boosted OER electrocatalysis. *J. Energy Chem.* **2023**, *76*, 195–213. https://doi.org/10.1016/j.jechem.2022.09.022.
9. Mohammed-Ibrahim, J. A review on NiFe-based electrocatalysts for efficient alkaline oxygen evolution reaction. *J. Power Sources* **2020**, *448*, 227375. https://doi.org/10.1016/j.jpowsour.2019.227375.
10. Hoang, V.C.; Dave, K.; Gomes, V.G. Carbon quantum dot-based composites for energy storage and electrocatalysis: Mechanism, applications and future prospects. *Nano Energy* **2019**, *66*, 104093. https://doi.org/10.1016/j.nanoen.2019.104093.
11. Zhang, S.; Wang, L.; Xie, T.; Chen, Q.; Peng, W.; Li, Y.; Zhang, F.; Fan, X. Heterointerface enhanced NiFe LDH/V–Co_4N electrocatalysts for the oxygen evolution reaction. *J. Mater. Chem. A* **2022**, *10*, 21523–21530. https://doi.org/10.1039/d2ta04120k.
12. Wang, Y.; Yang, C.; Huang, Y.; Li, Z.; Liang, Z.; Cao, G. Nickel induced electronic structural regulation of cobalt hydroxide for enhanced water oxidation. *J. Mater. Chem. A* **2020**, *8*, 6699–6708. https://doi.org/10.1039/d0ta00010h.
13. Zhang, T.; Zhao, S.; Zhu, C.; Shi, J.; Su, C.; Yang, J.; Wang, M.; Li, J.; Li, J.; Liu, P.; et al. Rational construction of high-active Co3O4 electrocatalysts for oxygen evolution reaction. *Nano Res.* **2022**, *16*, 624–633. https://doi.org/10.1007/s12274-022-4879-2.

14. Alegre, C.; Busacca, C.; Di Blasi, A.; Di Blasi, O.; Aricò, A.S.; Antonucci, V.; Baglio, V. Electrocatalysis of Oxygen on Bifunctional Nickel-Cobaltite Spinel. *ChemElectroChem* **2020**, *7*, 124–130. https://doi.org/10.1002/celc.201901584.
15. Yang, J.; Xuan, H.; Yang, J.; Meng, L.; Wang, J.; Liang, X.; Li, Y.; Han, P. Metal-organic framework-derived FeS2/CoNiSe2 heterostructure nanosheets for highly-efficient oxygen evolution reaction. *Appl. Surf. Sci.* **2021**, *578*, 152016. https://doi.org/10.1016/j.apsusc.2021.152016.
16. Li, W.; Wu, L.; Wu, X.; Shi, C.; Li, Y.; Zhang, L.; Mi, H.; Zhang, Q.; He, C.; Ren, X. Regulation and mechanism study of the CoS2/Cu2S-NF heterojunction as highly-efficient bifunctional electrocatalyst for oxygen reactions. *Appl. Catal. B Environ.* **2022**, *303*, 120849. https://doi.org/10.1016/j.apcatb.2021.120849.
17. Wang, R.; Liu, B.; You, S.; Li, Y.; Zhang, Y.; Wang, D.; Tang, B.; Sun, Y.; Zou, J. Three-dimensional Ni3Se4 flowers integrated with ultrathin carbon layer with strong electronic interactions for boosting oxygen reduction/evolution reactions. *Chem. Eng. J.* **2021**, *430*, 132720. https://doi.org/10.1016/j.cej.2021.132720.
18. Zhang, X.; Pan, H.W.; Jia, Y.B.; Zhang, Y.; Jiang, Z.G.; Li, C.J.; Li, X.; Bao, L.H.; Ma, R.G.; Wang, K.K. Flower-like MOF-74 nanocomposites directed by selenylation towards high-efficient oxygen evolution. *J. Colloid Interface Sci.* **2022**, *623*, 552–560. https://doi.org/10.1016/j.jcis.2022.04.181.
19. Fan, X.M.; Ma, Y.X.; Sun, A.K.; Zhang, X.; Tang, L.; Guo, J.X. Engineering heterogeneous nickel-iron oxide/iron phosphate on P, N co-doped carbon fibers for efficient oxygen evolution reaction in neutral and alkaline solutions. *Surf Interfaces* **2021**, *25*, 101193. https://doi.org/10.1016/j.surfin.2021.101193.
20. Jia, Y.; Zhu, L.; Pan, H.; Liao, Y.; Zhang, Y.; Zhang, X.; Jiang, Z.; Chen, M.; Wang, K. Excellent electrocatalytic hydrogen evolution performance of hexagonal NiCoP porous nanosheets in alkaline solution. *Appl. Surf. Sci.* **2022**, *580*, 152314. https://doi.org/10.1016/j.apsusc.2021.152314.
21. Lu, Z.; Cao, Y.; Xie, J.; Hu, J.; Wang, K.; Jia, D. Construction of Co2P/CoP@Co@NCNT rich-interface to synergistically promote overall water splitting. *Chem. Eng. J.* **2022**, *430*, 132877. https://doi.org/10.1016/j.cej.2021.132877.
22. Zhang, G.G.; Wang, X.C. Oxysulfide semiconductors for photocatalytic overall water splitting with visible light. *Angew. Chem. Int. Ed. Engl.* **2019**, *58*, 15580–15582. https://doi.org/ 10.1002/anie.201909669.
23. Ishikawa, A.; Takata, T.; Kondo, J.N.; Hara, M.; Kobayashi, H.; Domen, K. Oxysulfide $Sm_2Ti_2S_2O_5$ as a Stable Photocatalyst for Water Oxidation and Reduction under Visible Light Irradiation ($\lambda \leq 650$ nm). *J. Am. Chem. Soc.* **2002**, *124*, 13547–13553. https://doi.org/10.1021/ja0269643.
24. Mukherjee, P.; Sathiyan, K.; Vijay, A.K.; Bar-Ziv, R.; Zidki, T. Hybrid Nanostructure of Mixed Transition Metal Oxysulfides Supported by Porous PBA as Efficient Electrocatalysts for the Oxygen Evolution Reaction. *Isr. J. Chem.* **2021**, *62*, e202100110. https://doi.org/10.1002/ijch.202100110.
25. Wang, B.; Hu, Y.; Yu, B.; Zhang, X.; Yang, D.; Chen, Y. Heterogeneous CoFe–Co8FeS8 nanoparticles embedded in CNT networks as highly efficient and stable electrocatalysts for oxygen evolution reaction. *J. Power Sources* **2019**, *433*, 126688. https://doi.org/10.1016/j.jpowsour.2019.05.094.
26. Zheng, X.; Cao, Y.; Zheng, X.; Cai, M.; Zhang, J.; Wang, J.; Hu, W. Engineering Interface and Oxygen Vacancies of $Ni_xCo_{1-x}Se_2$ to Boost Oxygen Catalysis for Flexible Zn–Air Batteries. *ACS Appl. Mater. Interfaces* **2019**, *11*, 27964–27972. https://doi.org/10.1021/acsami.9b08424.
27. Moysiadou, A.; Lee, S.; Hsu, C.-S.; Chen, H.M.; Hu, X. Mechanism of Oxygen Evolution Catalyzed by Cobalt Oxyhydroxide: Cobalt Superoxide Species as a Key Intermediate and Dioxygen Release as a Rate-Determining Step. *J. Am. Chem. Soc.* **2020**, *142*, 11901–11914. https://doi.org/10.1021/jacs.0c04867.
28. Zhuang, L.; Jia, Y.; Liu, H.; Wang, X.; Hocking, R.K.; Liu, H.; Chen, J.; Ge, L.; Zhang, L.; Li, M.; et al. Defect-Induced Pt–Co–Se Coordinated Sites with Highly Asymmetrical Electronic Distribution for Boosting Oxygen-Involving Electrocatalysis. *Adv. Mater.* **2019**, *31*, e1805581. https://doi.org/10.1002/adma.201805581.
29. Qin, J.-F.; Yang, M.; Chen, T.-S.; Dong, B.; Hou, S.; Ma, X.; Zhou, Y.-N.; Yang, X.-L.; Nan, J.; Chai, Y.-M. Ternary metal sulfides MoCoNiS derived from metal organic frameworks for efficient oxygen evolution. *Int. J. Hydrogen Energy* **2020**, *45*, 2745–2753. https://doi.org/10.1016/j.ijhydene.2019.11.156.
30. Bai, Y.; Wang, Y.; Qiao, Z.; Yang, Y.; Deng, L.; Li, C.; Chen, X.; Wang, S.; Huang, Y.; Zhang, X.; et al. Facile synthesis of Fe_2P/Co embedded trifunctional electrocatalyst for high-performance anion exchange membrane fuel cells, rechargeable Zn–air batteries, and overall water splitting. *J. Mater. Chem. A* **2022**, *10*, 16037–16045. https://doi.org/10.1039/d2ta03099c.
31. Su, H.; Song, S.; Gao, Y.; Li, N.; Fu, Y.; Ge, L.; Song, W.; Liu, J.; Ma, T. In Situ Electronic Redistribution Tuning of $NiCo_2S_4$ Nanosheets for Enhanced Electrocatalysis. *Adv. Funct. Mater.* **2022**, *32*, 2109731. https://doi.org/10.1002/adfm.202109731.
32. Anantharaj, S.; Kundu, S.; Noda, S. "The Fe Effect": A review unveiling the critical roles of Fe in enhancing OER activity of Ni and Co based catalysts. *Nano Energy* **2021**, *80*, 105514. https://doi.org/10.1016/j.nanoen.2020.105514.
33. Wang, X.; Xiao, H.; Li, A.; Li, Z.; Liu, S.; Zhang, Q.; Gong, Y.; Zheng, L.; Zhu, Y.; Chen, C.; et al. Constructing NiCo/Fe_3O_4 Heteroparticles within MOF-74 for Efficient Oxygen Evolution Reactions. *J. Am. Chem. Soc.* **2018**, *140*, 15336–15341. https://doi.org/10.1021/jacs.8b08744.

34. Gao, W.-K.; Yang, M.; Chi, J.-Q.; Zhang, X.-Y.; Xie, J.-Y.; Guo, B.-Y.; Wang, L.; Chai, Y.-M.; Dong, B. In situ construction of surface defects of carbon-doped ternary cobalt-nickel-iron phosphide nanocubes for efficient overall water splitting. *Sci. China Mater.* **2019**, *62*, 1285–1296. https://doi.org/10.1007/s40843-019-9434-7.
35. Du, J.; You, S.; Li, X.; Tang, B.; Jiang, B.; Yu, Y.; Cai, Z.; Ren, N.; Zou, J. In Situ Crystallization of Active NiOOH/CoOOH Heterostructures with Hydroxide Ion Adsorption Sites on Velutipes-like CoSe/NiSe Nanorods as Catalysts for Oxygen Evolution and Cocatalysts for Methanol Oxidation. *ACS Appl. Mater. Interfaces* **2020**, *12*, 686–697. https://doi.org/10.1021/acsami.9b16626.
36. Liu, T.; Asiri, A.M.; Sun, X. Electrodeposited Co-doped $NiSe_2$nanoparticles film: A good electrocatalyst for efficient water splitting. *Nanoscale* **2016**, *8*, 3911–3915. https://doi.org/10.1039/c5nr07170d.
37. Du, J.; Zou, Z.; Liu, C.; Xu, C. Hierarchical Fe-doped Ni_3Se_4 ultrathin nanosheets as an efficient electrocatalyst for oxygen evolution reaction. *Nanoscale* **2018**, *10*, 5163–5170. https://doi.org/10.1039/c8nr00426a.
38. Yang, J.; Zhu, G.; Liu, Y.; Xia, J.; Ji, Z.; Shen, X.; Wu, S. Fe_3O_4-Decorated Co_9S_8 Nanoparticles In Situ Grown on Reduced Graphene Oxide: A New and Efficient Electrocatalyst for Oxygen Evolution Reaction. *Adv. Funct. Mater.* **2016**, *26*, 4712–4721. https://doi.org/10.1002/adfm.201600674.
39. Zhu, M.; Zhou, Y.; Sun, Y.; Zhu, C.; Hu, L.; Gao, J.; Huang, H.; Liu, Y.; Kang, Z. Cobalt phosphide/carbon dots composite as an efficient electrocatalyst for oxygen evolution reaction. *Dalton Trans.* **2018**, *47*, 5459–5464. https://doi.org/10.1039/c7dt04291d.
40. Yuan, M.; Dipazir, S.; Wang, M.; Sun, Y.; Gao, D.; Bai, Y.; Zhang, M.; Lu, P.; He, H.; Zhu, X.; et al. Polyoxometalate-assisted formation of CoSe/$MoSe_2$ heterostructures with enhanced oxygen evolution activity. *J. Mater. Chem. A* **2019**, *7*, 3317–3326. https://doi.org/10.1039/c8ta11976g.
41. Thambidurai, M.; Kim, J.Y.; Song, J.; Ko, Y.; Muthukumarasamy, N.; Velauthapillai, D.; Lee, C. Nanocrystalline Ga-doped ZnO thin films for inverted polymer solar cells. *Sol. Energy* **2014**, *106*, 95–101. https://doi.org/10.1016/j.solener.2013.12.009.
42. Xu, X.J.; Li, J.Y.; Zhang, C.H.; Zhang, S.C.; Su, G.; Shi, Z.C.; Wang, H.L.; Huang, M.H. Controllable transition engineering from homogeneous $NiSe_2$ nanowrinkles to heterogeneous Ni_3Se_4/$NiSe_2$ rod-like nanoarrays for promoted urea-rich water oxidation at large current densities. *Appl. Catal. B.* **2022**, *319*, 121949. https://doi.org/10.1016/j.apcatb.2022.121949.
43. Chen, H.; Fan, M.; Li, C.; Tian, G.; Lv, C.; Chen, D.; Shu, K.; Jiang, J. One-pot synthesis of hollow NiSe–CoSe nanoparticles with improved performance for hybrid supercapacitors. *J. Power Sources* **2016**, *329*, 314–322. https://doi.org/10.1016/j.jpowsour.2016.08.097.
44. Liu, Z.; Jia, R.; Chen, F.; Yan, G.; Tian, W.; Zhang, J.; Zhang, J. Electrochemical process of early-stage corrosion detection based on N-doped carbon dots with superior Fe3+ responsiveness. *J. Colloid Interface Sci.* **2021**, *606*, 567–576. https://doi.org/10.1016/j.jcis.2021.08.058.
45. Li, N.; Bediako, D.K.; Hadt, R.G.; Hayes, D.; Kempa, T.J.; von Cube, F.; Bell, D.C.; Chen, L.X.; Nocera, D.G. Influence of iron doping on tetravalent nickel content in catalytic oxygen evolving films. *Proc. Natl. Acad. Sci. USA* **2017**, *114*, 1486–1491. https://doi.org/10.1073/pnas.1620787114.
46. Wang, P.; Luo, Y.; Zhang, G.; Wu, M.; Chen, Z.; Sun, S.; Shi, Z. MnO_x-Decorated Nickel-Iron Phosphides Nanosheets: Interface Modifications for Robust Overall Water Splitting at Ultra-High Current Densities. *Small* **2022**, *18*, 2105803. https://doi.org/10.1002/smll.202105803.
47. Wang, P.; Qi, J.; Chen, X.; Li, C.; Li, W.; Wang, T.; Liang, C. Three-Dimensional Heterostructured NiCoP@NiMn-Layered Double Hydroxide Arrays Supported on Ni Foam as a Bifunctional Electrocatalyst for Overall Water Splitting. *ACS Appl. Mater. Interfaces* **2020**, *12*, 4385–4395. https://doi.org/10.1021/acsami.9b15208.